Bio-inspired neuromuscular reflex based hopping controller for a segmented robotic leg

Bioinspiration & Biomimetics

OPEN ACCESS

RECEIVED
25 July 2019

REVISED
23 December 2019

ACCEPTED FOR PUBLICATION
22 January 2020

PUBLISHED
24 February 2020

PAPER

Bio-inspired neuromuscular reflex based hopping controller for a segmented robotic leg

Guoping Zhao[1], **Florian Szymanski and Andre Seyfarth**

Lauflabor Locomotion Laboratory, Institute of Sport Science, Centre for Cognitive Science, Technical University of Darmstadt, Magdalenenstr 27, Darmstadt, 64289, Germany

[1] Author to whom any correspondence should be addressed.

E-mail: zhao@sport.tu-darmstadt.de

Keywords: bio-inspired, neuromuscular, reflex, hopping, legged robot

Supplementary material for this article is available online

Abstract

It has been shown that human-like hopping can be achieved by muscle reflex control in neuromechanical simulations. However, it is unclear if this concept is applicable and feasible for controlling a real robot. This paper presents a low-cost two-segmented robotic leg design and demonstrates the feasibility and the benefits of the bio-inspired neuromuscular reflex based control for hopping. Simulation models were developed to describe the dynamics of the real robot. Different neuromuscular reflex pathways were investigated with the simulation models. We found that stable hopping can be achieved with both positive muscle force and length feedback, and the hopping height can be controlled by modulating the muscle force feedback gains with the return maps. The force feedback neuromuscular reflex based controller is robust against body mass and ground impedance changes. Finally, we implemented the controller on the real robot to prove the feasibility of the proposed neuromuscular reflex based control idea. This paper demonstrates the neuromuscular reflex based control approach is feasible to implement and capable of achieving stable and robust hopping in a real robot. It provides a promising direction of controlling the legged robot to achieve robust dynamic motion in the future.

1. Introduction

The legged locomotion found in humans and animals are energetic, versatile, and robust against perturbations. The functionality of the leg can be separated into three locomotor sub-functions, which are stance (axial leg function), swing (rotational leg function), and balance (trunk posture control) [1]. The stance sub-function is to support body weight and create the centre of mass bouncing behavior (e.g. during walking, running, etc). Although human leg structure and the locomotion control are complex, highly simplified template models emphasizing the elastic stance leg function can describe and reproduce some basic characteristics of human walking and running gait [2–4]. Hopping can be considered as a primitive motion which focuses on the stance sub-function. A better understanding of how hopping motion is generated and controlled can help us further recognize the basic principles of human locomotion.

In general, the models proposed for explaining the stance leg function can be divided into two levels: mechanical level and neuromuscular level. Mechanical level models simplify the neuromuscular properties of major muscle groups in the stance leg and represent the stance leg function as a mechanical spring. For instance, a constant stiffness prismatic spring used in the spring loaded inverted pendulum (SLIP) template model is one of the simplest representations of the stance leg sub-function for dynamic locomotion (e.g. hopping, walking, running, etc) [2, 4]. However, the constant stiffness spring model cannot describe the perturbation behaviors because it is energy conservative. Therefore, a few extended SLIP models were proposed. For instance, the ESLIP [5] model and VSLIP [6] model modulate the spring stiffness and/or rest length during the locomotion to regulate the system energy.

The neuromuscular level models include the muscle properties (e.g. force-length and force-velocity relationship) and neural reflexes (e.g. muscle force, length,

and velocity reflex). For instance, a two-segmented model with a point mass and a Hill-type extensor muscle was proposed in [7] to explain the functionality of the positive force feedback in bouncing gaits. Recently, this model was used with linear reflex compositions for investigating the sensor-motor maps [8]. A further simplified model which ignores the leg geometric properties was used for demonstrating the role of intrinsic muscle properties and reflexes in generating stable hopping [9, 10]. With multi-segment and multi-muscle complex models, Geyer *et al* showed that human-like stable and rich bipedal locomotion can be achieved with neural networks emphasizing muscle reflexes [11, 12]. The neuromuscular reflex based controller proposed for these complex models have also been implemented on lower limb prostheses [13, 14] and exoskeletons [15, 16] to assist human walking.

Compared to the mechanical level models, neuromuscular level models provide deeper insights on the potential benefits of muscle properties and the neural reflex control for generating bouncing gaits (e.g. hopping, walking, running, etc). Although the hopping motion has been extensively studied with the simulation models mentioned above, it is unclear if the control concept is applicable and feasible for controlling a real hopping robot because most of the time the physical properties of the leg (e.g. leg inertia, foot-ground collision model, damping in the joint, etc) are ignored in the simplified models. Therefore, in this paper, we focus on investigating if the bio-inspired neuromuscular reflex based controller can generate stable hopping in both the realistic simulation model and the real robot.

Lots of legged robots emphasizing the bouncing leg function were developed during the last few decades. They can be divided into three groups based on the actuator types: (i) serial elastic actuators (SEAs, e.g. [17–19]), (ii) soft actuators (e.g. pneumatic actuators [20–22]), (iii) quasi-direct-drive (QDD) actuators (e.g. electric motors with low gear ratio gearboxes [23–26]). The intrinsic impedance in the SEAs and soft actuators can be beneficial for reducing the energetic cost and impact forces. However, it is hard to modulate the intrinsic impedance during the motion. For the QDD actuators, we can control the impedance and emulate different actuator dynamics (e.g. springs, Hill-type muscles, etc) with a virtual model control approach [27]. In addition, QDD actuators can potentially transfer kinetic energy back to electric energy by regenerative braking [23]. Therefore, the QDD actuators were chosen for the robotic leg in this study.

The goal of this paper is to develop a low-cost robotic leg for hopping and demonstrate the benefits of the bio-inspired neuromuscular reflex based controller in both simulation and hardware experiments. In the following section, we first introduce the robot hardware design and simulation environment (section 2). Then the bio-inspired neuromuscular reflex based hopping controller is presented in section 3. Sections 4 and 5 present the design of the experiments and the results of the simulation and hardware experiments which demonstrates the feasibility and benefits of the bio-inspired controller. Section 6 discusses the results and gives insights about this study and future work.

2. Robot hardware design and simulation

2.1. Mechanical design

The single leg robot consists of two brushless direct current (BLDC) motors (E8318-120KV, Hymotor, China) which control the hip and knee joint separately in the sagittal plane (figures 1(A) and (B)). The leg is serially actuated. To minimize the leg moment of inertia, the hip and knee motors are co-axially located at the top of the thigh. Knee joint is coupled with the knee motor shaft by a rope-pulley mechanism (gear-ratio 4:1). In order to avoid high mechanical stiffness and friction in the transmission chain, no gearbox is used for the motors. The direct-drive for the hip and the QDD for the knee actuation ensures the transparency between the motor and the external environment [24]. This makes it possible to achieve relative good torque control performance by motor current sensing (without any force/torque sensors).

Carbon fiber tubes were chosen as the thigh and shank segments to withstand high loads while keeping the weight and the moment of inertia low. All other mechanical parts, except the screws and bearings, were 3D printed with plastic materials (PLA and ABS) to further reduce the robot weight and keep the cost low. The robot hip is fixed on a 1D linear guide rail so that we can focus on the leg extension function for hopping. The total mass of the robot is 2.8 kg. The thigh and shank segment lengths are 0.27 m.

To test if the design is also suitable for bipedal hopping, a bipedal robot was built by connecting two single robotic legs with a trunk (figures 1(C) and (D)). This is important for multi-legged robots because the individual leg function in the robot may be different between both legs which would result in performance deficits (e.g. asymmetric leg function during hopping). Similar to the single leg robot, the trunk motion is also constrained in 1D (up and down movement) by a linear bearing. The total mass of the bipedal robot is 6.2 kg. To keep the maximum knee joint torque to robot mass ratio similar as the single leg robot, the gear-ratio of the bipedal robot leg knee motors (rope-pulley mechanism) is designed as 5:1. The rest of the mechanical design of the leg is the same as the single leg robot.

2.2. Control system architecture

In the single leg hopping robot, each motor is equipped with an incremental encoder (AMT102-V, CUI, USA) to measure the motor angle. The encoders are used for both low-level current control (motor driver MTVESC50A, Maytech, China) and high-level reflex based control. The motor driver runs low-level field oriented control (FOC) at 20 kHz. A force-sensing resistor is mounted underneath the foot to detect

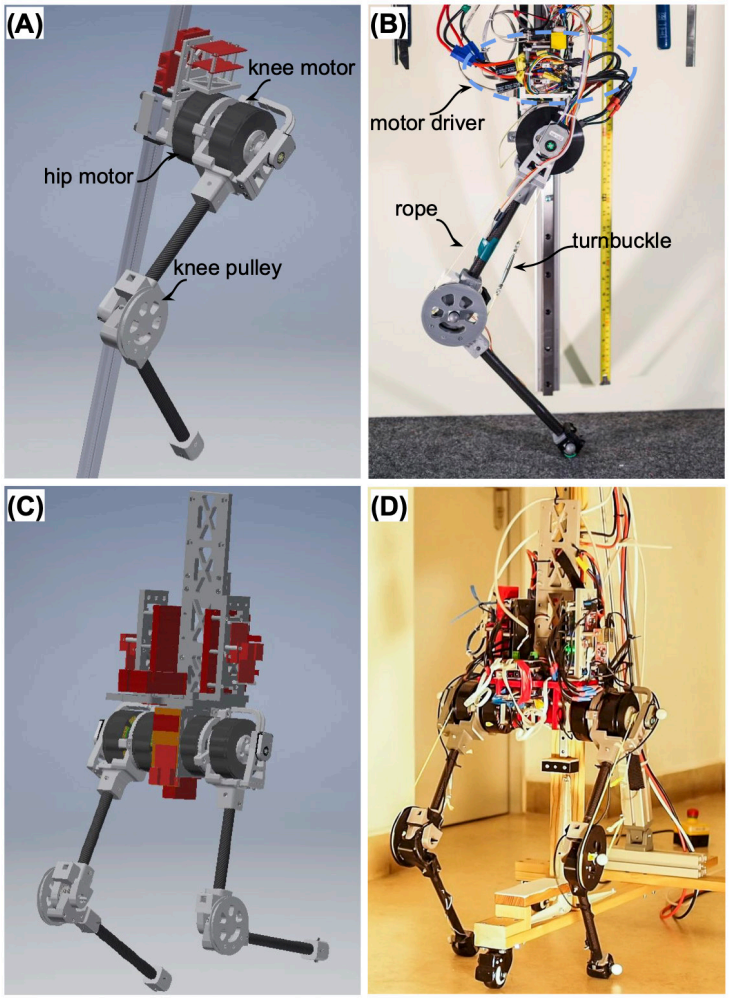

Figure 1. GURO robotic leg mechanical design. (A) The single leg robot CAD model (without ropes and electronic parts). (B) A photo of the single leg robot. (C) The bipedal robot CAD model (without ropes). (D) A photo of the bipedal robot.

if the robot is in the stance phase or flight phase. An ESP32s microcontroller reads all the sensor data and sends the data to the high-level controller. The high-level controller is implemented in realtime at 1 kHz with Matlab Simulink xPC target (Matlab R2018a, Mathworks, USA). The motor drivers and the microcontrollers are interfaced with the xPC target machine through EtherCAT communication bus at 1 kHz. Except the xPC target machine, which is off-board to the robot, all the components described here are onboard. The overview of the control system architecture is illustrated in figure 2.

The bipedal robot has the same control architecture as the single leg robot. The main difference is the motor driver. In order to generate higher torques in the motors, the motor drivers in the bipedal robot (FSESC6.6, Flipsky, China) are able to deliver about twice the amount of peak current compared to the motor drivers in the single leg robot.

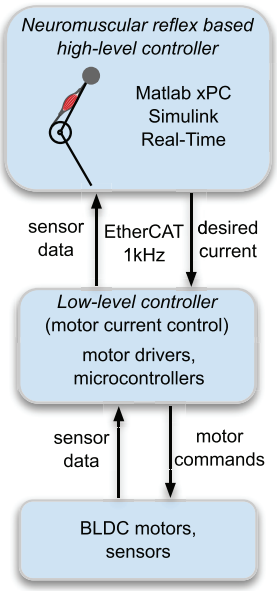

Figure 2. GURO robot control system architecture.

2.3. Simulation

We built a physical simulation model in MuJoCo [28] based on the robot CAD design. Each part of the robot was weighted before the assembling. The moment of inertia of every part was calculated based on the measured weight by assuming the density

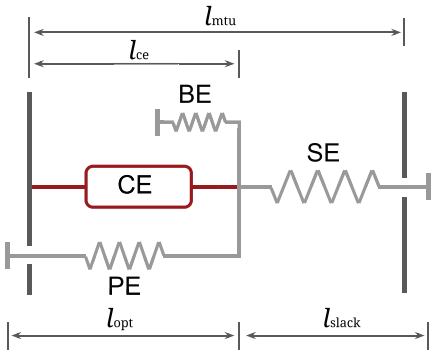

Figure 3. Muscle-tendon unit (MTU) model. CE, BE, PE and SE denote contractile element, buffer elasticity, parallel elasticity, and series elasticity, respectively.

was homogeneous. In order to get realistic foot-ground contact model parameters and joint damping coefficients for the simulation, the real robot experiment hopping height data (range from 0.02 m to 0.12 m) were used to manually tune those parameters. Initially, by assuming a relatively stiff ground and low joint damping coefficients in the simulation, the simulation model showed higher hopping height than the real robot. Then we manually tuned those parameters iteratively till the simulation model exhibited similar hopping behaviors and hopping heights as the real robot. The MuJoCo physical simulation model runs at 10 kHz to ensure stable and accurate simulations. The control rate in the simulation was set to 1 kHz to match the control rate of the real robot.

3. Controller

3.1. Muscular model

The Hill-type muscle-tendon unit (MTU) model (figure 3 [11]), is used in this paper. The MTU consists of a series elasticity (SE), a contractile element (CE), a parallel elasticity (PE), and a buffer elasticity (BE). The generated CE force F_{ce} is computed by the muscle activation (A), maximum isometric force F_{max}, force-length (f_l) and force-velocity (f_v) relationships of the CE [7, 11]:

$$F_{ce} = AF_{max} f_l\left(l_{ce}\right) f_v\left(v_{ce}\right) \tag{1}$$

$$f_l\left(l_{ce}\right) = \exp\left(c\left|\frac{l_{ce}-l_{opt}}{l_{opt}w}\right|\right) \tag{2}$$

$$f_v\left(v_{ce}\right) = \begin{cases} \frac{v_{max}-v_{ce}}{v_{max}+Kv_{ce}} & v_{ce} < 0 \\ N+(N-1)\frac{v_{max}-v_{ce}}{7.56Kv_{ce}-v_{max}} & v_{ce} \geqslant 0 \end{cases} \tag{3}$$

where negative CE velocity v_{ce} denotes the concentric movement. The width w and residual force factor c define the shape of f_l. The eccentric force enhancement N and the shape factor K define the f_v. The MTU force F_m can be computed as

$$F_m = F_{se} = F_{ce} + F_{pe} - F_{be} \tag{4}$$

where

$$F_{se} = \begin{cases} F_{max}\left(\frac{l_{se}/l_{slack}-1}{\varepsilon_{ref}}\right)^2 & l_{se} > l_{slack} \\ 0 & l_{se} \leqslant l_{slack} \end{cases} \tag{5}$$

$$F_{pe} = F_{max}\left(\frac{l_{ce}-l_{opt}}{l_{opt}\varepsilon_{pe}}\right)^2 \tag{6}$$

$$F_{be} = F_{max}\left(\frac{l_{min}-l_{ce}}{l_{opt}\varepsilon_{be}}\right)^2 \tag{7}$$

and l_{se} is the SE length, l_{slack} is the SE rest length, ε_{ref} is the reference strain of the SE, ε_{pe} is the reference strain of the PE, l_{opt} is the optimum length, l_{min} is the BE rest length, ε_{be} is the BE reference strain. All the parameter values are listed in the appendix table A3. They are taken from previous studies [7, 11] and adapted to the robot.

3.2. Neural reflex

The muscle excitation-contraction coupling (ECC) is modelled as [7]:

$$\tau\frac{\mathrm{d}A(t)}{\mathrm{d}t} = S(t) - A(t) \tag{8}$$

where $S(t)$ is the stimulation signal (neural input), $A(t)$ is the muscle activation, and τ is a time constant. We assume a linear relation between S and the sensory feedback P (i.e. F_m, l_{ce}, v_{ce}):

$$S(t) = \begin{cases} S_0 & t \leqslant \Delta t \\ S_0 + GP(t-\Delta t) & t > \Delta t \end{cases} \tag{9}$$

where S_0 is the constant stimulation bias, G is the gain factor for different feedback signals, and Δt is the sensory feedback time delay. $S(t)$ is saturated in the range of $[0, 1]$. This linear assumption is a common approach to represent the sensory feedback mechanism [7, 8, 11]. In the implementation, each sensory feedback P signal (i.e. F_m, l_{ce}, v_{ce}) is normalized. More specifically, $S(t)$ for each individual feedback pathway (i.e. force feedback (FFB), length feedback (LFB), and velocity feedback (VFB)) is computed as:

$$S(t) = \begin{cases} S_0 & t \leqslant \Delta t \\ S_0 + G_F F_m^n(t-\Delta t) & \text{FFB}, t > \Delta t \\ S_0 + G_L l_{ce}^n(t-\Delta t) & \text{LFB}, t > \Delta t \\ S_0 + G_F v_{ce}^n(t-\Delta t) & \text{VFB}, t > \Delta t \end{cases} \tag{10}$$

where $F_m^n = F_m/F_{max}$, $l_{ce}^n = l_{ce}/l_{opt}$, and $v_{ce}^n = v_{ce}/v_{max}$. G_F, G_L, and G_V denote the gain for force, length, and velocity feedback pathway, respectively. Compared to the other approaches [7, 9, 10], the length and velocity offsets are not taken into account in the feedback pathways because finding the optimal control parameters for a certain motion is not the aim of this paper. Here, we aim at demonstrating the feasibility and potential benefits of the neuromuscular reflex control concept on the robotic hardware system.

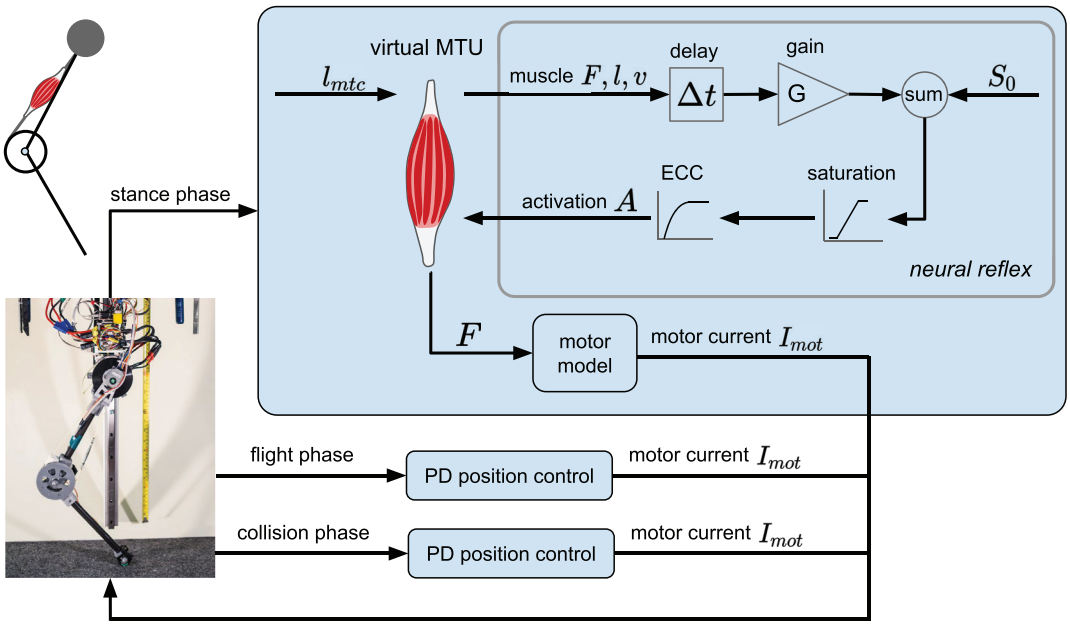

Figure 4. Schematic view of the hopping controller. The force sensor underneath the foot is used to detect if the robot is in stance, flight or collision phase.

3.3. Hopping control scheme

The hopping controller is separated into flight, stance, and collision phase. The overview of the control scheme for a single leg is shown in figure 4. The individual leg control scheme of the bipedal robot is the same as the single leg robot.

3.3.1. *Stance phase*

In the stance phase, the hip motor is set to free (desired current set to 0 A) while the knee motor is controlled as a virtual Hill-type MTU (figures 3 and 4). The virtual MTU only produces knee extension torque during the stance phase. The virtual MTU length l_{mtc} is calculated as

$$l_{mtc} = r_{mtc}\,\theta^k_{mot} \Big/ c \tag{11}$$

where θ^k_{mot}, c and r_{mtc} are the robot knee motor angle measured by the encoder, the gear ratio, and the virtual MTC moment arm, respectively. c is 4, which is the ratio between knee joint pulley diameter and the knee motor pulley diameter. r_{mtc} is set to 0.04 m in this study. The muscle activation A is calculated based on the neural reflex controller. Virtual muscle states (i.e. muscle F, l, v) are computed based on the muscular model given l_{mtc}. The knee motor desired current I^k_{mot} is calculated and sent to the motor driver based on the motor model given the desired virtual MTC force.

3.3.2. *Flight phase*

The flight phase controller is used to prepare the leg with an appropriate posture for the next landing. Here, a simple PD position controller with fixed target knee and hip angles is used during the flight phase. The PD values are manually tuned so that the robot can not only achieve the desired posture before next touch down (TD) but also have low effective joint compliance to avoid high impact forces at TD. In this study, the hip and knee desired joint angles during the flight phase are set to 20° and 40°, respectively. The controller switches from stance phase control to flight phase control if the knee angle reaches 40° or the force sensor underneath the foot detects no contact forces.

3.3.3. *Collision phase*

The collision phase is defined as a very short time duration t_c after TD. Both hip and knee motor are position controlled with relatively low P but high D values to absorb the impact energy during the collision. Due to relatively high P values in the hip and knee motor flight PD position controller, the robot shank starts rebounding/oscillating if the robot lands on stiff ground. The collision phase control can absorb the impact and prevent the undesired oscillations after landing. We set t_c as 20 ms because it is much shorter than the muscle reflex time (around 200 ms for hopping) while the shank rebound can still be eliminated.

3.4. Implementation

The hopping control scheme was implemented with Matlab Simulink (2018a) in both simulation and the real-time controller for the real robots at 1 kHz control rate. The simulation model foot-ground contact parameters and the joint damping coefficients were manually tuned (see detailed description in section 2.3). The gains for different reflex pathways will be described later for each experiment. The parameters for the PD position controller during the flight phase and the collision phase were tuned by hand. The desired motor currents were saturated

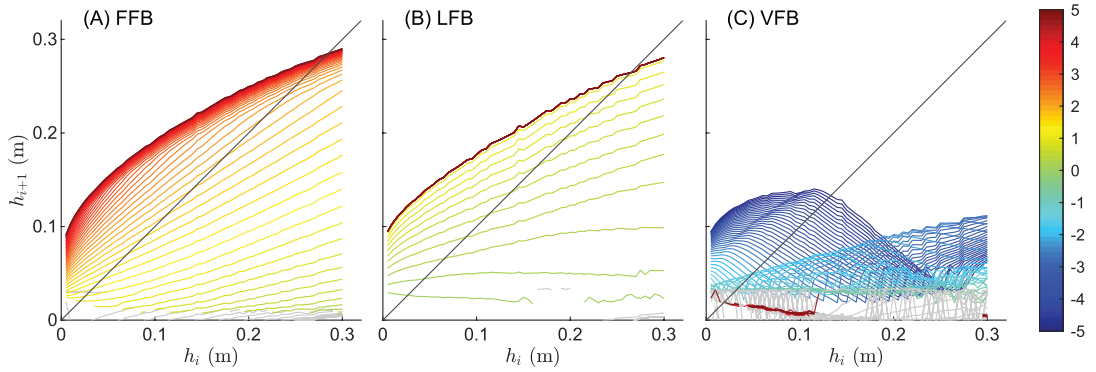

Figure 5. Simulation results of the return maps of the bipedal robot. (A) With only force feedback (FFB). (B) With only length feedback (LFB). (C) With only velocity feedback (VFB). The range of FFB, LFB and VFB gain is $[-5, 5]$ with a step size of 0.1. Different gain values are denoted with different colors. The light grey color denotes the situation which the robot does not rebound. The intersections of the colored line and the dark grey diagonal line indicate fixed points (periodic motions, i.e. $h_{i+1} = h_i$). The periodic motion is stable if the slope $S = \mathrm{d}h_{i+1}/\mathrm{d}h_i$ around the fixed point satisfies the condition $|S| < 1$. h_i and h_{i+1} denote the ith and the $(i+1)$th hopping height, respectively.

due to the motor driver hardware limitation. The maximum motor current was 50 A and 100 A for the single leg robot and the bipedal robot, respectively. A lithium polymer battery was used to delivery high enough peak currents to the motor drivers. Both simulation and the real-time controller have the same parameter values because the simulation model is very close to the hardware setup.

4. Experiments

This section presents the design of the experiments in both simulations and robot hardware systems. First, in order to show if stable hopping can be achieved with the proposed bio-inspired hopping controller, the return maps of the individual muscle reflexes are computed. Then the robustness of the muscle force feedback is demonstrated by comparing the return maps of different robot model properties and ground properties. Finally, the robot hardware experiments were conducted to verify the simulation model and prove the feasibility of the hardware design and implementation.

4.1. Return maps

In order to investigate the influence of the individual muscle feedback pathway (i.e. force, length and velocity) on the hopping motion, we computed return maps for each feedback pathway with brute force in simulation by dropping the robot from 0.005 m to 0.3 m height with a step size of 0.005 m. The hopping height zero is defined as the robot hip height at TD. The range of the feedback gain was chosen as $[-5, 5]$ because the robot can generate both stable hopping and landing (not rebound) motion within this range.

4.2. Robustness of the FFB

To explore the robustness of the neuromuscular reflex based controller, we analyzed the effects of parameters of the model and the environment on the return map. For the robot parameters, we increased the robot mass from the original mass m to $1.6 \times m$ with a step size of $0.2 \times m$. We also investigated the influences of the rope impedance on the hopping performance. We changed the rope from the original rigid configuration (stiffness 8×10^7 N m^{-1}, damping coefficient 500 Ns m^{-1}) to stiff (10^6 N m^{-1}, 5 Ns m^{-1}), moderate (10^5 N m^{-1}, 5 Ns m^{-1}) and soft (10^4 N m^{-1}, 5 Ns m^{-1}) configurations. In this case, the rope can be considered as an elastic component in serial of the virtual MTU. For the environment parameters, we decreased the ground impedance from the original impedance (scaled as 1) to 0.4 with a step size of 0.2. Here we focus on how the FFB return map changes. Based on the original FFB return map (shown in figure 5(A)), the robot will not rebound if the gain is smaller than 0.5. And the robot hopping height will be saturated if the gain is larger than 2.5. Therefore, the FFB return map with the gain in $[0.5, 2.5]$ (step size 0.1) was computed for different body mass, ground impedance, and rope stiffness conditions.

4.3. Robot hardware demonstration

The bio-inspired neuromuscular reflex based controller (figure 4) was implemented on the real robot. To validate the simulation model, the stable hopping height was compared between the real robot and the simulation model with different FFB gains. The real robot hopping height was measured by a high-speed camera based motion capture system (Qualisys, Sweden). Ten continuous stable hopping data in each FFB gain were used to calculate the mean and the standard deviation of the real robot hopping height. The robot does not have a stable hopping pattern if the FFB gain is smaller than 1.1. The pelvis range of motion is limited by the linear guide length which is 0.4 m. In addition, considering the strength and durability of the 3D printed plastic parts (e.g.

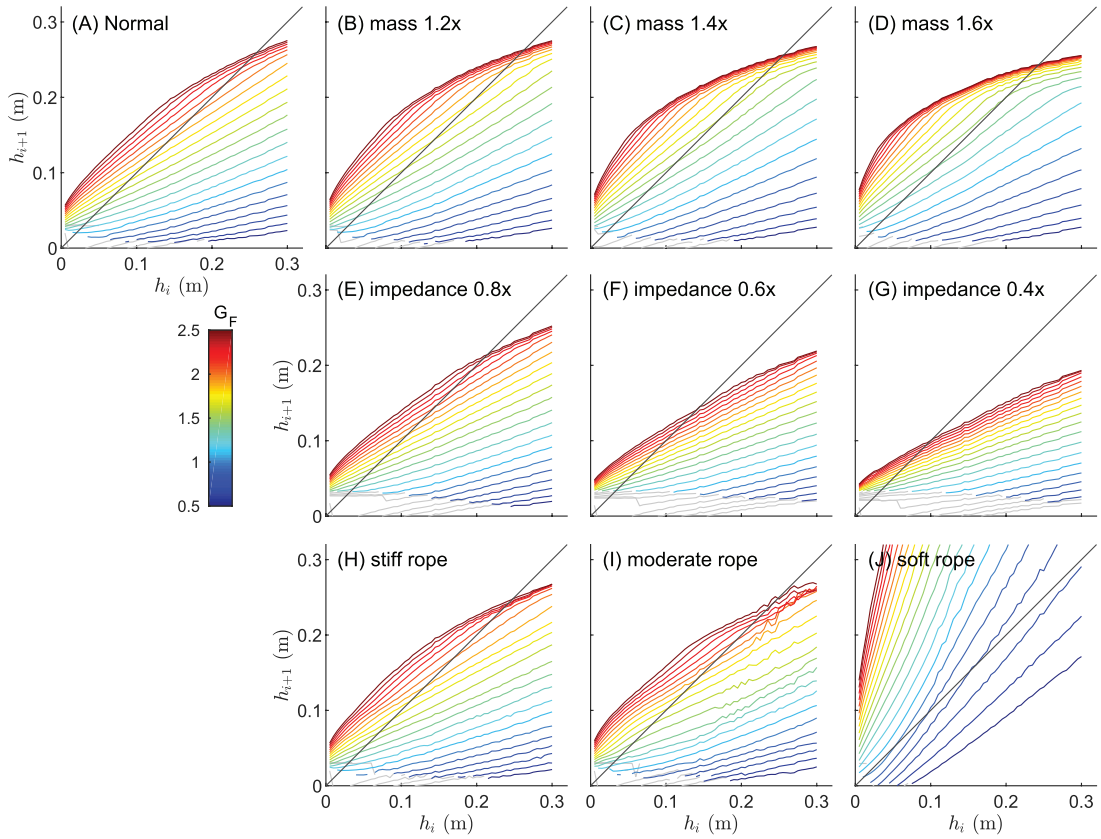

Figure 6. The bipedal robot simulation results of the return maps with only FFB in different conditions. (A) The reference condition. The scaled body mass is 1. The ground is rigid (scaled impedance is 1). And the rope is also rigid (stiffness $k_{rope} = 8 \times 10^7$ N m^{-1}, damping coefficient $d_{rope} = 500$ Ns m^{-1}). (B)–(D) are the return maps of different body mass conditions. The scaled body masses for (B)–(D) are 1.2, 1.4 and 1.6, respectively. (E)–(G) are the return maps of different ground impedance. The scaled impedance are 0.8, 0.6 and 0.4 for (E)–(G), respectively. (H)–(J) are the return maps of different rope stiffness. The rope stiffness for (H)–(J) are 10^6 N m^{-1}, 10^5 N m^{-1}, 10^4 N m^{-1}, respectively. The rope damping coefficients for all three conditions are set as 5 Ns m^{-1}. The range of FFB gain G_F is [0.5, 2.5] with a step size of 0.1. Different gain values are denoted with different colors. The light grey color denotes the situation which the robot does not rebound. The intersections of the colored line and the dark grey diagonal line indicate fixed points (periodic motions, i.e. $h_{i+1} = h_i$). The periodic motion is stable if the slope $S = \mathrm{d}h_{i+1}/\mathrm{d}h_i$ around the fixed point satisfies the condition $|S| < 1$. h_i and h_{i+1} denote the ith and the $(i+1)$th hopping height, respectively.

knee shafts, motor pulleys, etc), we only did the robot hopping experiments with the FFB gain from 1.1 to 1.8 with a step size of 0.1.

5. Results

Because the results of the single leg robot and the bipedal robot are very similar, we only present the results of the bipedal robot.

5.1. Return maps

The return maps of each feedback pathway (i.e. FFB, LFB and VFB) are shown in figure 5. The results shows that both positive FFB (G_F), positive LFB (G_L) and negative VFB (G_V) can generate stable hopping. The lines (each line corresponds to one feedback gain) in the FFB return map are smoother than the lines in the return map of LFB and VFB. The VFB generate unstable and chaotic motions if the G_V is around -1.2. There is a clear saturation trend in the maximum stable hopping height h_{max} for all three feedback pathways (when $G_F > 2.5$, $G_L > 1.0$ or $G_V < -4.5$). The FFB has the highest h_{max} (0.28 m, $G_F = 5$) compared to the LFB (0.27 m, $G_F = 5$) and the VFB (0.13 m, $G_V = -5$). In the FFB, the robot will not rebound even with the 0.3 m dropping height if the G_F is less than zero.

The FFB shows superior features (e.g. smoothness, range of stable hopping height, stability) compared to the LFB and VFB (figure 5). Therefore in the following analysis, we will only focus on the FFB.

5.2. Robustness of the FFB

The FFB return maps with different body mass, ground impedance and rope stiffness conditions are shown in figure 6. Compared to the FFB return map in the normal condition (figure 6(A)), the robot maximum stable hopping height decreases with the increasing body mass or decreasing ground impedance. Compared to different ground impedance and rope stiffness conditions, the return maps in the different body mass conditions are more similar to the normal condition in terms of the stable hopping height and the shape of the map. For instance, the maximum stable hopping height only dropped 0.016 m from

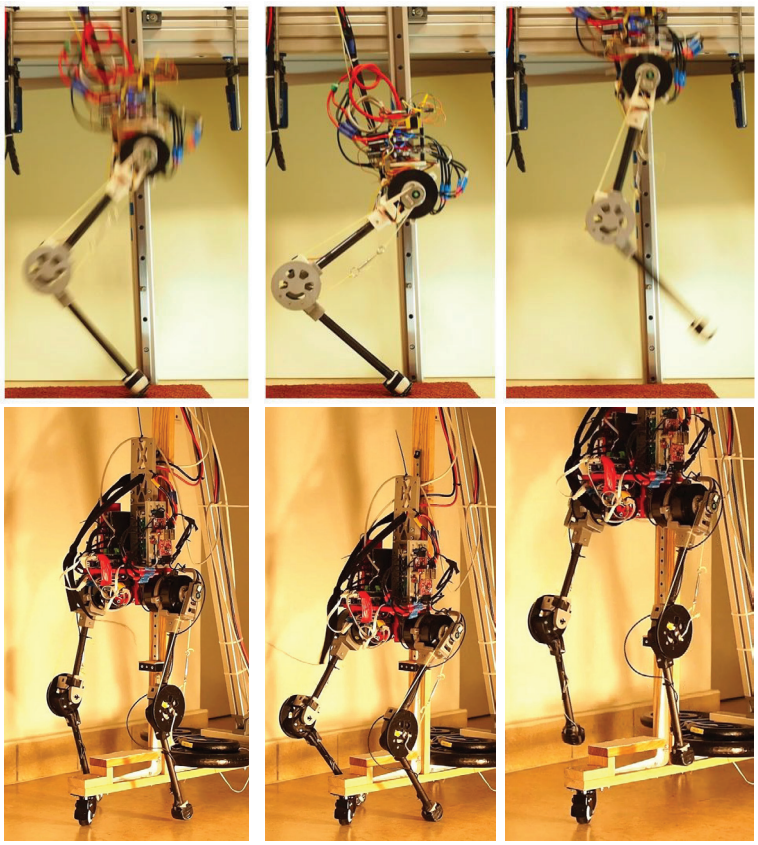

Figure 7. Snapshots of the single leg robot and the bipedal robot during hopping.

the normal condition to the 1.6 times body mass condition. For the different ground impedance conditions, the robot shows stable hopping solutions. However, the maximum stable hopping height drops a lot with decreasing ground impedance compared to the normal condition. The maximum stable hopping height for normal, 0.8 impedance, 0.6 impedance, and 0.4 impedance are 0.26 m, 0.215 m, 0.145 m, and 0.102 m, respectively. The return map in the stiff rope condition is almost the same as the normal condition. It gets a bit unstable in the moderate rope stiffness condition. In the soft rope condition, there is no stable hopping solution in the hopping height from 0 to 0.3 m.

5.3. Robot hardware demonstration

Both the single leg and the bipedal robot can achieve stable and robust hopping with appropriate feedback gains (figure 7, see the supplementary video for more details (stacks.iop.org/BB/15/026007/mmedia)). The real robot hopping behavior is very similar to the hopping behavior we observed from the simulation. The comparison between the stable hopping height of the real robot and the simulation model with different FFB gains are shown in figure 8. The hopping height of both simulation and the real robot experiments increases with higher FFB gain. The maximum hopping height difference is 0.008 m at $G_F = 1.6$. The difference between the simulation and experimental hopping height are 0.004 ± 0.002 m (mean$\pm$ standard deviation). This confirms that the simulation model is valid. Note that the simulation parameters

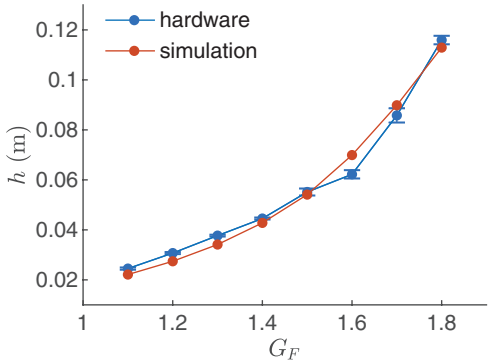

Figure 8. The bipedal robot stable hopping height (h) with different force feedback gains (G_F). The blue and red color denote mean hopping height in the robot hardware experiments and the simulations, respectively. The blue error bars denote ± 1 standard deviation of the experimental data. The means and standard deviations of the robot hopping height of each G_F were calculated with ten continuous stable hopping heights. The simulation hopping height standard deviations are not plotted because they are very small (less than 0.01 mm).

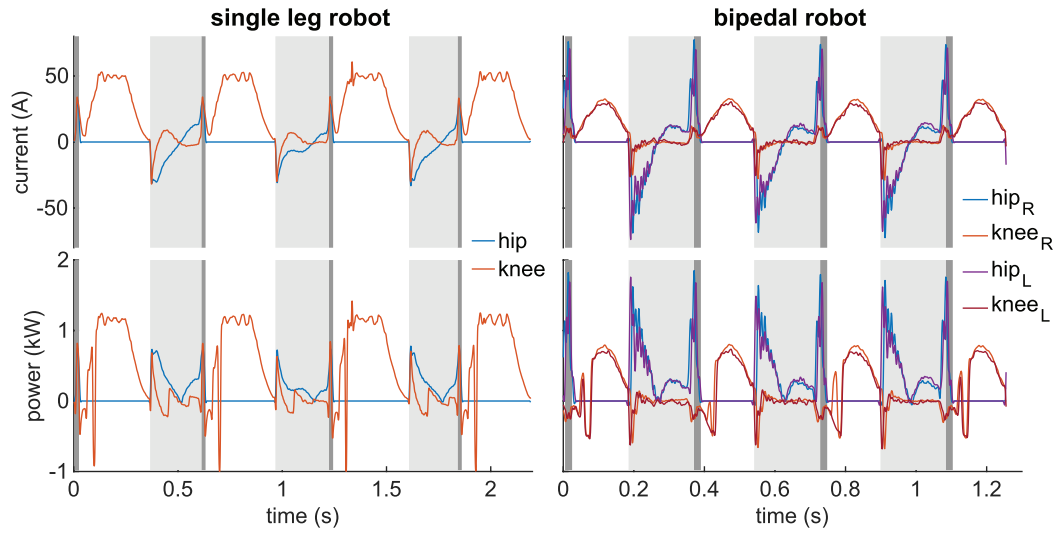

Figure 9. The measured motor current and the electric power consumption of the single leg robot and the bipedal robot during hopping at the hopping height of 4 cm. Light grey and dark grey areas denote the flight phase and the collision phase, respectively. Different colors denote different motors. For the bipedal robot, the subscripts $_R$ and $_L$ denote the right leg and the left leg, respectively. Positive current is defined as the current which results in extension torque in the robot hip or knee joint. Negative power indicates the regenerative braking (charging the battery). Both current and power data are low-pass filtered with a cutoff frequency of 100 Hz (fourth-order Butterworth filter).

(i.e. foot-ground contact parameters and joint damping coefficients) were manually tuned to fit the data (see detailed description in section 2.3).

The measured motor current and the electric power consumption of the single leg robot and the bipedal robot during hopping at the hopping height of 4 cm are shown in figure 9. The single leg knee motor current is saturated at 50 A (due to the motor driver hardware limitation) during the mid-stance phase. We need to increase the motor driver maximum current and/or the gear ratio if we want to achieve higher hopping height. The hip motor peak current in the bipedal robot reaches around 90 A at the beginning and the end of the flight phase. This is because of relative large P value in the PD control of the hip motor. The knee motor of both the single leg robot and the bipedal robot show regenerative braking at the beginning of stance phase and the beginning of flight phase. The average electric energy consumption for each knee motor is 40 J per hop. This is relatively high because the motor operated in low speed high current (inefficient, high heat loss) condition. It is required to avoid gear boxes which would cause additional moment of inertia and undesired side effects due to friction. The regenerated energy is 30% of the consumption energy in each knee motor. The hip motors do not have regenerative braking phases.

6. Discussion

In this paper, we presented a low-cost robotic leg design which is capable of demonstrating the bio-inspired neuromuscular reflex based hopping controller. Based on the return maps from the simulation results, we found that the stable hopping can be achieved with both positive force and length reflex while the velocity reflex could result in unstable behaviors. The force reflex based control is more stable than the length reflex based control. The robustness of the force reflex based control was investigated by varying the model parameters (body mass and rope stiffness) and the ground impedance in the simulation. The robot hardware experimental results show that the bio-inspired controller is feasible to implement and capable of achieving stable and robust hopping with the proposed low-cost robotic leg.

Recently, it has been more and more popular to use QDD electric motors in legged robots for dynamic locomotion [23–26, 29]. The planetary gearbox with low gear ratio is often used in QDD actuators because the motor direct torque output is small. Here, instead of planetary gearboxes, the rope-pulley mechanism was used in our robotic leg to achieve similar effects as the gearbox. The pulleys used in the robot were 3D printed with plastics. This reduces the mass and the cost of the robot. In addition, it also enables fast prototyping and testing with different gear ratios.

Compared to the robots which use customized high torque density motors (e.g. MIT Cheetah [23] and MIT Cheetah 3 [30], the torque output of the motor used in our robot is relatively low because we are using off the shelf motors and motor drivers. For instance, the max knee torque of our bipedal robot is 40 N m while the max torque of the MIT cheetah 3 actuator is 230 N m). Therefore the robot was built with 3D printed plastic parts and carbon tubes to minimize the weight and the cost. The robot experimental results prove that the motor is capable of delivering enough torque to generate hopping motion. The robot has been tested for more than 1000 hops with different hopping heights

(from 2 cm to 12 cm). No mechanical failure occurred. This demonstrates that the robot design is robust and can be used as a test platform for investigating dynamic legged locomotion. Because we used 3D printed parts and off the shelf motors and motor drivers, the total cost of one robotic leg is less than 600 Euros (excluding the battery and the PC for controlling the robot). This low-cost design makes it more accessible for research and education in legged robotics.

Compared to the mechanical spring or spring-damper based virtual model control (e.g. [26, 31–33]), the proposed bio-inspired control inherits the intrinsic muscle dynamics and neuroreflex properties which can be beneficial for stabilizing the motion [9, 10] and simplifying the high level control by muscle reflexes (FFB, LFB and VFB) [8, 11, 12]. The return maps of the FFB, LFB and VFB demonstrate that both FFB and LFB can result in stable hopping motion and can be used for controlling the robot hopping height (figure 5). This is in line with the findings from the simplified point mass simulation models [7, 8, 10]. These findings also indicate that, for the stance phase control, the neuromuscular reflex properties play a more important role than the leg inertia properties (a point mass model was used in [7, 8]) and the leg geometry (a prismatic leg was used in [10]) in shaping the hopping behavior. Further analysis on the change of the FFB return maps with different body masses and ground impedance (figure 6) highlights the robustness of the neuromuscular FFB based hopping controller. Therefore the proposed bio-inspired neuromuscular reflex based control approach can potentially be implemented on other legged robots to achieve bouncing gait without too much tuning of the control parameters. Note that the length and velocity offsets were not taken into account in the feedback pathways in this study. In the future, investigating the influences of the offsets on the return maps could help us find better hopping behavior with LFB and VFB.

Adding an elastic component in serial of the actuator can be beneficial in terms of energy efficiency and stability for dynamic legged locomotion [17, 34]. However, the results of different rope stiffness (with only FFB, figure 6) show that the additional elastic component in serial of the virtual MTU can lead to unstable hopping if the serial component is too soft. Other control approaches (e.g. combining different reflexes, modulating feedback gains during the stance phase) are required to have a stable hopping in this condition.

In this study, we focused on the neuromuscular reflex based hopping controller during the stance phase. A PD position control was used in the flight phase. This results in high current peaks in the motors at the beginning and the end of flight phase. In future research, the robot flight phase PD control could be replaced by the neuromuscular reflex control to solve this issue. And the current 1D hopping controller can potentially be transferred to 2D hopping (i.e. hopping forward and backward) by tuning the flight phase control. Besides, the MTU model used in this study could potentially be replaced by a simplified model with fewer parameters (e.g. linearized Hill model from [35]) in the future. This could be helpful in optimizing the hopping performance.

Another limitation of this study is that we investigated the hopping with individual reflex pathways (i.e. force, length, and velocity). With a simplified simulation model, it has been shown that the hopping performance (e.g. hopping height, efficiency, robustness, etc) can be improved by linear combinations of different reflexes [8]. In addition, combining the muscle reflex control and the feed forward stimulation could help to generate and stabilize hopping motion [10]. These different combinations could be investigated in the future.

Table A1. Single leg robot physical parameters.

Parameter	Value (unit)
Total mass	2.8 kg
Hip mass	1.24 kg
Thigh mass	1.38 kg
Shank mass	0.18 kg
Thigh length	0.27 m
Shank length	0.27 m
Thigh moment of inertia w.r.t hip joint axis	8.7×10^{-3} kg m^2
Shank moment of inertia w.r.t knee joint axis	1.8×10^{-3} kg m^2
Motor rotor moment of inertia w.r.t motor axis	0.5×10^{-3} kg m^2
Knee motor pulley diameter	0.02 m
Knee joint pulley diameter	0.08 m
Hip joint range of motion	$[-70°, 70°]$
Knee joint range of motion	$[5°, 70°]$
Motor max torque τ_{max}	4 N m
Motor max speed ω_{max}	2600 rpm
Motor torque constant k_τ	0.08 Nm A^{-1}
Linear guide rail damping coefficient d_{rail}	0.027 Ns m^{-1}
Rope stiffness k_{rope}	1×10^8 N m^{-1}
Rope damping coefficient d_{rope}	500 Ns m^{-1}

Acknowledgments

This work was partially supported by the QSL program (Project ANSYMB, No. 00295) at Technische Universität Darmstadt and the DFG-Funded EPA Project under Grant No. AH307/2-1 and Grant No. SE1042/29-1.

Author contributions

Guoping Zhao is the main and corresponding author of this paper. Guoping Zhao developed the robotic leg, implemented the neuromuscular reflex based controller. Guoping Zhao and Florian Szymanski contributed the simulation and hardware robot experiments. Florian Szymanski built the bipedal robot and processed the

Table A2. Bipedal robot physical parameters.

Parameter	Value (unit)
Total mass	6.2 kg
Trunk mass	3.3 kg
Knee Rotor mass	0.26 kg
Thigh mass	1.0 kg
Shank mass	0.19 kg
Thigh length	0.27 m
Shank length	0.28 m
Thigh moment of inertia w.r.t hip joint axis	7.1×10^{-3} kg m^2
Shank moment of inertia w.r.t knee joint axis	1.7×10^{-3} kg m^2
Motor rotor moment of inertia w.r.t motor axis	0.35×10^{-3} kg m^2
Knee motor pulley diameter	0.02 m
Knee joint pulley diameter	0.1 m
Hip joint range of motion	$[-70°, 70°]$
Knee joint range of motion	$[0°, 115°]$
Motor max torque τ_{max}	8 N m
Motor max speed ω_{max}	2600 rpm
Motor torque constant k_τ	0.08 Nm A^{-1}
Linear guide rail damping coefficient d_{rail}	0.027 Ns m^{-1}
Rope stiffness k_{rope}	1×10^8 N m^{-1}
Rope damping coefficient d_{rope}	500 Ns m^{-1}

Table A3. Virtual neuromuscular model parameters.

Parameter	Value (unit)
F_{max}	1600 N
N	1.5
K	5
c	ln 0.05
w	0.4
l_{opt}	0.1 m
l_{slack}	0.4 m
l_{min}	$l_{opt} - w$
v_{max}	$12 l_{opt}$ s^{-1}
ε_{ref}	0.08
ε_{pe}	w
ε_{be}	$w/2$
S_0	0.01
τ	0.01 s
Δt	0.005 s

hardware experimental data. Guoping Zhao interpreted the results and drafted the manuscript. Andre Seyfarth contributed to conceptualizing of the work. All authors revised the manuscript.

Appendix

The detailed physical parameters of the single leg and the bipedal robot are shown in the tables A1 and A2, respectively.

The virtual neuromuscular model parameter values are listed in table A3. The parameter values were adopted from previous studies [7, 11]. The muscle maximum isometric force F_{max} was scaled to the robot weight. The time delay Δt was adapted to 0.005 s to have better hopping behavior in the robot.

ORCID iDs

Guoping Zhao https://orcid.org/0000-0002-1908-5388

References

[1] Seyfarth A *et al* 2013 Biomechanical, neuromechanical concepts for legged locomotion: computer models and robot validation *Routledge Handbook of Motor Control and Motor Learning* pp 99–119
[2] Blickhan R 1989 The spring-mass model for running and hopping *J. Biomech.* **22** 1217–27
[3] Full R and Koditschek D 1999 Templates and anchors: neuromechanical hypotheses of legged locomotion on land *J. Exp. Biol.* **202** 3325–32
[4] Geyer H, Seyfarth A and Blickhan R 2006 Compliant leg behaviour explains basic dynamics of walking and running *Proc. R. Soc.* B **273** 2861–7
[5] Ludwig C, Grimmer S, Seyfarth A and Maus H-M 2012 Multiple-step model-experiment matching allows precise definition of dynamical leg parameters in human running *J. Biomech.* **45** 2472–5
[6] Riese S and Seyfarth A 2011 Stance leg control: variation of leg parameters supports stable hopping *Bioinspiration Biomimetics* **7** 016006
[7] Geyer H, Seyfarth A and Blickhan R 2003 Positive force feedback in bouncing gaits? *Proc. R. Soc.* B **270** 2173–83
[8] Schumacher C and Seyfarth A 2017 Sensor-motor maps for describing linear reflex composition in hopping *Frontiers Comput. Neurosci.* **11** 108
[9] Haeufle D F B, Grimmer S and Seyfarth A 2010 The role of intrinsic muscle properties for stable hopping stability is achieved by the force velocity relation *Bioinspiration Biomimetics* **5** 016004
[10] Haeufle D F B, Grimmer S, Kalveram K-T and Seyfarth A 2012 Integration of intrinsic muscle properties, feed-forward and feedback signals for generating and stabilizing hopping *J. R. Soc. Interface* **9** 1458–69
[11] Geyer H and Herr H 2010 A muscle-reflex model that encodes principles of legged mechanics produces human walking dynamics and muscle activities *IEEE Trans. Neural Syst. Rehabil. Eng.* **18** 263–73
[12] Song S and Geyer H 2015 A neural circuitry that emphasizes spinal feedback generates diverse behaviours of human locomotion *J. Physiol.* **593** 3493–511
[13] Eilenberg M F, Geyer H and Herr H 2010 Control of a powered ankle-foot prosthesis based on a neuromuscular model *IEEE Trans. Neural Syst. Rehabil. Eng.* **18** 164–73
[14] Thatte N and Geyer H 2016 Toward balance recovery with leg prostheses using neuromuscular model control *IEEE Trans. Biomed. Eng.* **63** 904–13
[15] Ruiz Garate V, Parri A, Yan T, Munih M, Molino Lova R, Vitiello N and Ronsse R 2016 Walking assistance using artificial primitives: a novel bioinspired framework using motor primitives for locomotion assistance through a wearable cooperative exoskeleton *IEEE Robot. Autom. Mag.* **23** 83–95
[16] Wu A R, Dzeladini F, Brug T J H, Tamburella F, Tagliamonte N L, van Asseldonk E H F, van der Kooij H and Ijspeert A J 2017 An adaptive neuromuscular controller for assistive lower-limb exoskeletons: a preliminary study on subjects with spinal cord injury *Frontiers Neurorobot.* **11** 30

[17] Sharbafi M A, Rode C, Kurowski S, Scholz D, Möckel R, Radkhah K, Zhao G, Rashty A M, von Stryk O and Seyfarth A 2016 A new biarticular actuator design facilitates control of leg function in BioBiped3 *Bioinspiration Biomimetics* **11** 046003
[18] Zhu Q, Mao Y, Xiong R and Wu J 2016 Adaptive torque and position control for a legged robot based on a series elastic actuator *Int. J. Adv. Robot. Syst.* **13** 26
[19] Heim S, Ruppert F, Sarvestani A A and Spröwitz A 2018 Shaping in practice: training wheels to learn fast hopping directly in hardware *2018 IEEE Int. Conf. on Robotics and Automation* pp 1–6
[20] Raibert M H 1986 *Legged Robots that Balance* (Cambridge, MA: MIT press)
[21] Niiyama R, Nagakubo A and Kuniyoshi Y 2007 Mowgli: a bipedal jumping and landing robot with an artificial musculoskeletal system *Proc. IEEE Int. Conf. on Robotics and Automation* pp 2546–51
[22] Liu X, Rosendo A, Ikemoto S, Shimizu M and Hosoda K 2018 Robotic investigation on effect of stretch reflex and crossed inhibitory response on bipedal hopping *J. R. Soc. Interface* **15** 20180024
[23] Seok S, Wang A, Chuah M Y, Hyun D J, Lee J, Otten D M, Lang J H and Kim S 2015 Design principles for energy-efficient legged locomotion and implementation on the MIT cheetah robot *IEEE/ASME Trans. Mechatronics* **20** 1117–29
[24] Kenneally G, De A and Koditschek D E 2016 Design principles for a family of direct-drive legged robots *IEEE Robot. Autom. Lett.* **1** 900–7
[25] Ding Y and Park H 2017 Design and experimental implementation of a quasi-direct-drive leg for optimized jumping *2017 IEEE/RSJ Int. Conf. on Intelligent Robots and Systems* pp 300–5
[26] Kalouche S 2017 GOAT: a legged robot with 3D agility and virtual compliance *IEEE/RSJ Int. Conf. on Intelligent Robots and Systems* pp 4110–7
[27] Pratt J, Chew C-M, Torres A, Dilworth P and Pratt G 2001 Virtual model control: an intuitive approach for bipedal locomotion *Int. J. Robot. Res.* **20** 129–43
[28] Todorov E, Erez T and Tassa Y 2012 Mujoco: a physics engine for model-based control *IEEE/RSJ Int. Conf. on Intelligent Robots and Systems* pp 5026–33
[29] Kau N, Schultz A, Ferrante N and Slade P 2019 Stanford Doggo: an open-source, quasi-direct-drive quadruped *IEEE/RSJ Int. Conf. on Robotics and Automation* pp 6309–15
[30] Bledt G, Powell M J, Katz B, Di Carlo J, Wensing P M and Kim S 2018 MIT cheetah 3: design and control of a robust, dynamic quadruped robot *IEEE/RSJ Int. Conf. on Intelligent Robots and Systems* pp 2245–52
[31] Kalveram K T, Haeufle D F B, Seyfarth A and Grimmer S 2012 Energy management that generates terrain following versus apex-preserving hopping in man and machine *Biol. Cybern.* **106** 1–13
[32] Oehlke J, Sharbafi M A, Beckerle P and Seyfarth A 2016 Template-based hopping control of a bio-inspired segmented robotic leg *6th IEEE Int. Conf. on Biomedical Robotics and Biomechatronics* pp 35–40
[33] Hubicki C, Grimes J, Jones M, Renjewski D, Spröwitz A, Abate A and Hurst J 2016 Atrias: design and validation of a tether-free 3D-capable spring-mass bipedal robot *Int. J. Robot. Res.* **35** 1497–521
[34] Spröwitz A, Tuleu A, Vespignani M, Ajallooeian M, Badri E and Ijspeert A J 2013 Towards dynamic trot gait locomotion: design, control, and experiments with Cheetah-cub, a compliant quadruped robot *Int. J. Robot. Res.* **32** 932–50
[35] Council G, Yang S and Revzen S 2014 Deadbeat control with (almost) no sensing in a hybrid model of legged locomotion *Proc. of the Int. Conf. on Advanced Mechatronic Systems* pp 475–80